

# International Journal of Damage Mechanics

<http://ijd.sagepub.com>

---

## **Micromechanics-based Interfacial Debonding Model for Damage of Functionally Graded Materials with Particle Interactions**

G. H. Paulino, H. M. Yin and L. Z. Sun

*International Journal of Damage Mechanics* 2006; 15; 267

DOI: 10.1177/1056789506060756

The online version of this article can be found at:  
<http://ijd.sagepub.com/cgi/content/abstract/15/3/267>

---

Published by:



<http://www.sagepublications.com>

Additional services and information for *International Journal of Damage Mechanics* can be found at:

**Email Alerts:** <http://ijd.sagepub.com/cgi/alerts>

**Subscriptions:** <http://ijd.sagepub.com/subscriptions>

**Reprints:** <http://www.sagepub.com/journalsReprints.nav>

**Permissions:** <http://www.sagepub.co.uk/journalsPermissions.nav>

**Citations** <http://ijd.sagepub.com/cgi/content/refs/15/3/267>

# Micromechanics-based Interfacial Debonding Model for Damage of Functionally Graded Materials with Particle Interactions

G. H. PAULINO<sup>1</sup>, H. M. YIN<sup>1</sup> AND L. Z. SUN<sup>2,\*</sup>

<sup>1</sup>*Department of Civil and Environmental Engineering  
Newmark Laboratory, University of Illinois at Urbana-Champaign  
Urbana, IL 61801, USA*

<sup>2</sup>*Department of Civil and Environmental Engineering  
University of California, Irvine, CA 92697, USA*

**ABSTRACT:** A micromechanical damage model is developed for two-phase functionally graded materials (FGMs) considering the interfacial debonding of particles and pair-wise interactions between particles. Given an applied mechanical loading on the upper and lower boundaries of an FGM, in the particle–matrix zones, interactions from all other particles over the representative volume element (RVE) are integrated to calculate the homogenized elastic fields. A transition function is constructed to solve the elastic field in the transition zone. The progressive damage process is dependent on the applied loading and is represented by the debonding angles which are obtained from the relation between particle stress and interfacial strength. In terms of the elastic equivalency, debonded, isotropic particles are replaced by perfectly bonded, orthotropic particles. Correspondingly, the effective elasticity distribution in the gradation direction is solved. The computational implementation is discussed and numerical simulations are provided to illustrate the capability of the proposed model.

**KEY WORDS:** functionally graded materials (FGMs), micromechanical modeling, damage mechanics, interfacial debonding, pair-wise particle interaction.

---

\*Author to whom correspondence should be addressed. E-mail: lsun@uci.edu

## INTRODUCTION

**F**UNCTIONALLY GRADED MATERIALS (FGMs) have attracted significant attention from engineers due to their unique thermomechanical performance (Suresh and Mortensen, 1998; Miyamoto et al., 1999; Paulino et al., 2003). FGMs are generally manufactured by two phases of materials with different properties. Since the volume fraction of each phase gradually varies in the gradation direction, effective properties of FGMs change along this direction. Experimental observations (e.g., Sasaki and Hirai, 1991) show that the typical microstructure of FGMs, illustrated in Figure 1(a), contains a particle–matrix zone with dispersed particles filled in continuous matrix, followed by a skeletal transition zone in which the particle and matrix phases cannot be well defined because the two phases are interpenetrated into each other as a connected network. The transition zone is further followed by another particle–matrix zone with interchanged phases of particle and matrix.

While many FGMs are used in thermal protection systems, their mechanical behavior plays an important role in the design, application, and serviceability (Reiter et al., 1997). To simulate the mechanical responses of FGMs under certain loading conditions, FGMs are typically assumed to be homogenized materials with spatially varying effective material properties. To predict the effective elasticity distribution in the gradation direction, conventional composite models such as the Mori–Tanaka method and the

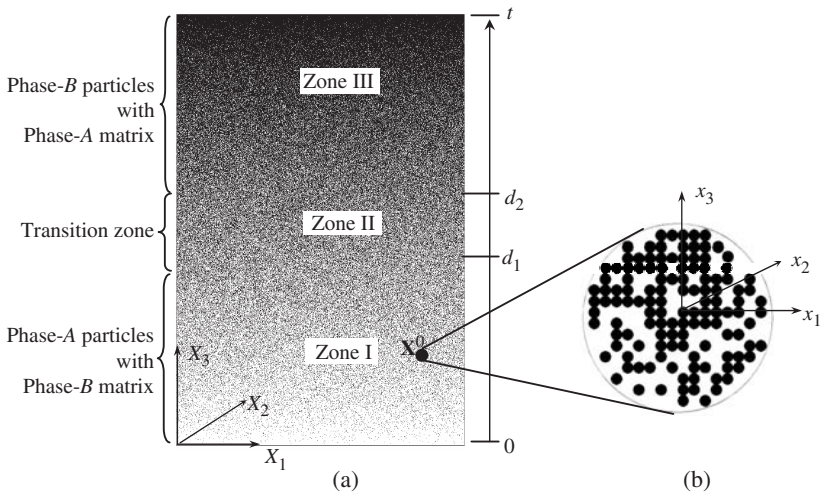


**Figure 1.** A two-phase FGM sample: (a) typical microstructure including A and B phases, and three zones; and (b) RVE of the neighborhood of the material point  $X^0$ .

self-consistent method were directly employed to estimate the effective elastic responses of FGMs (e.g., Zuiker, 1995; Reiter et al., 1997; Reiter and Dvorak, 1998; Suresh and Mortensen, 1998). Because they were originally developed for homogeneous mixtures with constant particle concentration, those models are not able to capture the material gradient nature of FGMs (Zuiker and Dvorak, 1994; Aboudi et al., 1999).

To this end, we have developed a micromechanics-based model (Yin et al. 2004, 2005) to predict the effective elasticity distribution in the gradation direction considering particle interaction and volume fraction distribution of phases. A novel formulation has been derived for the local elastic fields in the particle-matrix zone and a transition function has been constructed to make the homogenized elastic fields continuous and differentiable in the gradation direction. In the course of derivation, a microscopic representative volume element (RVE) is proposed to statistically represent the microstructure in the neighborhood of a material point in the particle-matrix zone.

Since the overall mechanical behavior of FGMs depends on microstructures including the heterogeneous constituents, their deformation and damage failure mechanisms are generally different from the monolithic material of each constituent. One of the predominant damage mechanisms is the interfacial debonding between the particles and matrix (Suresh et al., 1993). Prader and Degisher (1999) clearly observed particle debonding when the composites were subjected to an external loading. As seen in Figure 2(a), a particle is initially perfectly bonded to a continuous matrix. When the normal interfacial stress exceeds the interfacial strength due to external loading in the  $x_1$ -direction, the particle starts to debond from the matrix (Figure 2(b)). Then, the interfacial stress relaxes and the interfacial debonding may be stabilized. Thus, the damage results in the reduction in the effective stiffness of the overall material. For homogeneous composites, several analytical and/or numerical investigations on the effects of the interfacial debonding have been proposed in the literature, including, for instance, Jasiuk and Tong (1989), Qu (1993), Zhao and Weng (1996, 1997), Voyiadjis and Park (1997), Sangani and Mo (1997), Dvorak and Zhang (2001), Matous (2003), Sun et al. (2003), and Liu et al. (2004), among others. However, the effects of interfacial debonding on the effective behavior of FGMs have not been addressed yet.

Due to the graded microstructure, the local field in FGMs not only greatly changes between two phases, but also spatially varies in the gradation direction. Thus, interfacial debonding may only occur in some specific particles, and the magnitude of the damage also spatially depends on the location in the gradation direction. Debonding further changes the local field through particle interactions, so the damage evolution is fully coupled

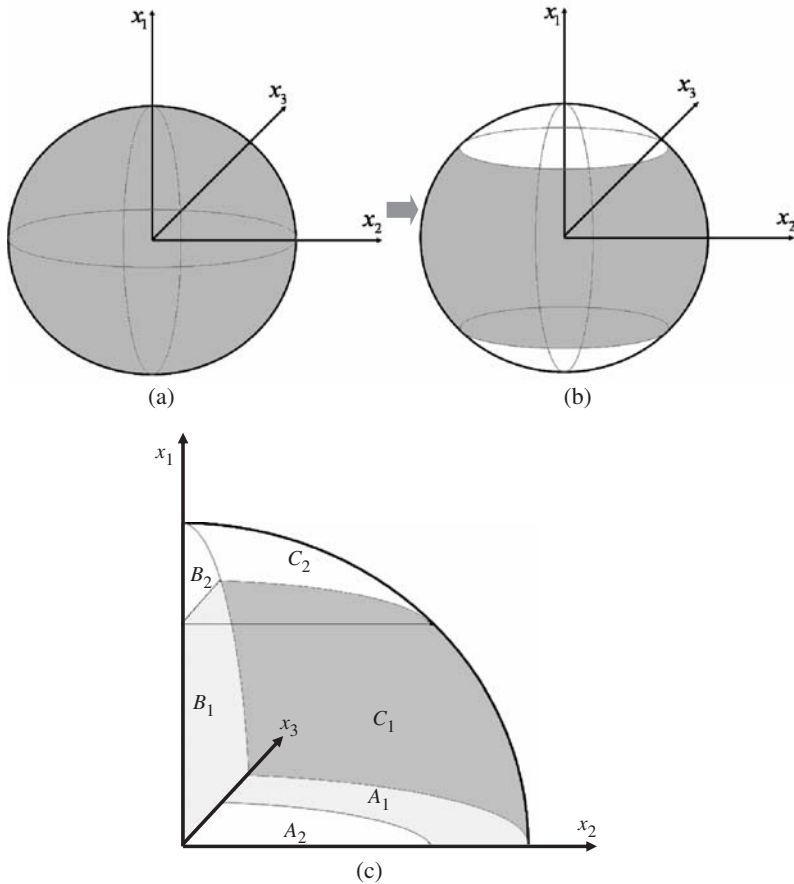


**Figure 2.** Schematic illustration for interfacial debonding of a spherical particle embedded in continuous matrix: (a) initially the particle is perfectly bonded to the matrix; (b) the particle is partially debonded from the matrix in the  $x_3$  direction; and (c) the debonded area is projected onto the three midplanes.

with the mechanical response in the gradation direction. Therefore, interfacial debonding of particles provides a significant effect on both the local fields in the microscopic scale and effective material properties in the macroscopic scale. In summary, we notice that the following issues due to interfacial debonding in FGMs need to be specifically considered:

- The damage of particles is spatially related to volume fraction distribution in the gradation direction of FGMs;
- The damage of particles is irreversible, so the effective properties of FGMs depend on the loading path;

- The evolution of interfacial debonding of particles is coupled with the local mechanical field.

Direct numerical simulations of interfacial debonding may provide a straightforward prediction about the local field changing with the damage evolution, but it is extremely expensive to model the complex microstructure of FGMs including many particles and to simulate the interfacial debonding with change in loading. The present study aims to develop a micro-mechanical damage model for investigating the damage effect of interfacial debonding on the effective elastic behavior of FGMs. For simplicity, both phases of FGMs are assumed to be isotropic and the particles are assumed to be spheres with identical radius. Given the interfacial strength between particle and matrix, we are able to determine the initiation of debonding at the interface. Partially debonded isotropic particles are then approximated by perfectly bonded orthotropic ones, with the orthotropic elastic tensor being determined by debonding angles. All particles with the same RVE are assumed to be identical so that they develop the same debonding angles. During the debonding process, pair-wise particle interactions are collected and the effective stress and strain distributions of each phase are calculated to derive the effective elasticity distribution in the gradation direction varying with the debonding evolution of particles. Finally, two types of specific loading conditions (uniaxial tension and shear loading) are simulated to demonstrate the capability of the proposed model.

This study is the very first step toward investigating damage of functionally graded particulate materials by means of a multiscale approach based on micromechanics principles. Essentially, it combines the techniques of Yin et al. (2004, 2005) and Liu et al. (2004). Although this preliminary investigation has several limitations, it offers a promising approach with room for further improvements. For instance, the modeling work on local failure of graded thermal barrier coatings under thermomechanical loading is underway.

## THE PAIR-WISE PARTICLE INTERACTION

Eshelby (1957) derived an analytical solution through a so-called equivalent inclusion method to solve the local elastic field of a single ellipsoidal particle embedded in the infinite domain under a far-field strain. The essence of this method is that the particle-matrix heterogeneous domain is transferred to a homogeneous domain which is the same as the matrix material but with an eigenstrain acting in the particle phase to represent elastic inhomogeneity. The equivalent inclusion method has been widely

applied in evaluating the effective mechanical properties of heterogeneous composites (Mura, 1987; Nemat-Nasser and Hori, 1999).

Based on Eshelby's equivalent inclusion method, the local strain field at a certain point  $\mathbf{x}$  in a particle embedded in the infinite matrix under the external far-field strain  $\boldsymbol{\varepsilon}^0$  is written as

$$\boldsymbol{\varepsilon}(\mathbf{x}) = \boldsymbol{\varepsilon}^0 + \boldsymbol{\varepsilon}'(\mathbf{x}), \quad (1)$$

where the perturbed strain  $\boldsymbol{\varepsilon}'$  due to the elastic mismatch between the particle and the matrix reads:

$$\boldsymbol{\varepsilon}'(\mathbf{x}) = - \int_{\Omega} \boldsymbol{\Gamma}(\mathbf{x}, \mathbf{x}') \cdot \mathbf{C}_0 : \boldsymbol{\varepsilon}^*(\mathbf{x}') d\mathbf{x}', \quad (2)$$

in which  $\Omega$  represents the ellipsoidal particle domain,  $\mathbf{C}_0$  the fourth rank elastic stiffness tensor of the matrix material, and  $\boldsymbol{\varepsilon}^*$  the equivalent eigenstrain due to the elastic mismatch. The symbols ' $\cdot$ ' and ' $:$ ' indicate the tensor contraction between two fourth-rank tensors and between fourth-rank and second-rank tensors, respectively. The modified two-point Green function  $\boldsymbol{\Gamma}$  has the form (Kröner, 1990):

$$\boldsymbol{\Gamma}_{ijkl}(\mathbf{x}, \mathbf{x}') = \frac{1}{16\pi\mu_0(1-\nu_0)} \left[ -\psi_{,ijkl} + (1-\nu) (\delta_{ik}\varphi_{,lj} + \delta_{il}\varphi_{,jk} + \delta_{jk}\varphi_{,il} + \delta_{jl}\varphi_{,ik}) \right] \quad (3)$$

with  $\psi = |\mathbf{x} - \mathbf{x}'|$ ,  $\varphi = 1/|\mathbf{x} - \mathbf{x}'|$ , and  $\mu_0$  and  $\nu_0$  being the shear modulus and Poisson's ratio of the matrix, respectively.

The stress equivalence in the spherical particle domain with elastic stiffness  $\mathbf{C}_1$  (Mura, 1987) demonstrates that

$$\mathbf{C}_1 : [\boldsymbol{\varepsilon}^0 + \boldsymbol{\varepsilon}'(\mathbf{x})] = \mathbf{C}_0 : [\boldsymbol{\varepsilon}^0 + \boldsymbol{\varepsilon}'(\mathbf{x}) - \boldsymbol{\varepsilon}^*(\mathbf{x})], \quad (4)$$

from which, the equivalent eigenstrain  $\boldsymbol{\varepsilon}^*$  is derived as

$$\boldsymbol{\varepsilon}^* = \mathbf{C}_0^{-1} \cdot (\mathbf{P}_0 - \Delta\mathbf{C}^{-1})^{-1} : \boldsymbol{\varepsilon}^0, \quad (5)$$

with  $\Delta\mathbf{C} = \mathbf{C}_1 - \mathbf{C}_0$  and

$$(\mathbf{P}_0)_{ijkl} = \frac{\delta_{ij}\delta_{kl} - (4-5\nu_0)(\delta_{ik}\delta_{jl} + \delta_{il}\delta_{jk})}{30\mu_0(1-\nu_0)}. \quad (6)$$

Combining Equations (1), (2), and (5), the local strain field  $\boldsymbol{\varepsilon}(\mathbf{x})$  can be calculated. In particular,  $\boldsymbol{\varepsilon}(\mathbf{x})$  in the spherical particle domain  $\Omega$  is shown to be uniform as

$$\boldsymbol{\varepsilon}(\mathbf{x}) = \bar{\boldsymbol{\varepsilon}} = (\mathbf{I} - \mathbf{P}_0 \cdot \Delta\mathbf{C})^{-1} : \boldsymbol{\varepsilon}^0, \tag{7}$$

with the fourth-rank identity tensor  $I_{ijkl} = (\delta_{ik}\delta_{jl} + \delta_{il}\delta_{jk})/2$ .

Moschovidis and Mura (1975) extended the single particle problem to the case of two interacting particles embedded in the infinite matrix domain. By expanding the equivalent eigenstrain and the disturbing strain in terms of polynomial form of local coordinates, we can solve Equations (1), (2), and (4) for the local strain field  $\boldsymbol{\varepsilon}(\mathbf{x})$ . Furthermore, the averaged strain in each spherical particle domain  $\Omega$  is integrated as:

$$\boldsymbol{\varepsilon} = [\mathbf{I} - \mathbf{P}_0 \cdot \Delta\mathbf{C} - \mathbf{P}(\mathbf{x}_1, \mathbf{x}_2) \cdot \Delta\mathbf{C}]^{-1} : \boldsymbol{\varepsilon}^0 + O(\rho^8), \tag{8}$$

where  $\rho = a/b$  and  $V_\Omega = 4\pi a^3/3$  (particle volume) with  $a$  being the particle radius and  $b$  being the center-to-center distance between the two particles centered at  $\mathbf{x}_1$  and  $\mathbf{x}_2$ , respectively. In addition, the fourth-rank tensor  $\mathbf{P}$  reads:

$$\begin{aligned} P_{ijkl}(\mathbf{x}_1, \mathbf{x}_2) = & \frac{\rho^3}{60\mu_0(1 - v_0)} [(5 - 3\rho^2)\delta_{ij}\delta_{kl} - (5 - 10v_0 + 3\rho^2)(\delta_{ik}\delta_{jl} + \delta_{il}\delta_{jk}) \\ & + 15(5 - 7\rho^2)n_i n_j n_k n_l - 15(1 - \rho^2)(\delta_{ij}n_k n_l + \delta_{kl}n_i n_j) \\ & - 15(v_0 - \rho^2)(\delta_{ik}n_j n_l + \delta_{jk}n_i n_l + \delta_{il}n_j n_k + \delta_{jl}n_i n_k)] \end{aligned} \tag{9}$$

with  $\mathbf{n} = (\mathbf{x}_1 - \mathbf{x}_2)/b$ . Comparing Equations (7) and (8), we can find that the additional particle provides an interaction on the averaged strain of the first particle as

$$\mathbf{d}(\mathbf{x}_1, \mathbf{x}_2) = \Delta\mathbf{C}^{-1} \cdot \mathbf{L}(\mathbf{x}_1, \mathbf{x}_2) : \boldsymbol{\varepsilon}^0 + O(\rho^8), \tag{10}$$

where the pair-wise interaction tensor is shown as

$$\mathbf{L}(\mathbf{x}_1, \mathbf{x}_2) = [\Delta\mathbf{C}^{-1} - \mathbf{P}_0 - \mathbf{P}(\mathbf{x}_1, \mathbf{x}_2)]^{-1} - [\Delta\mathbf{C}^{-1} - \mathbf{P}_0]^{-1}. \tag{11}$$

Ju and Chen (1994) have noted that the pair-wise interaction term can reach high precision as the order of  $O(\rho^8)$  where  $\rho$  is always no greater than 0.5. Furthermore, they also provided the mathematical inverse operation of the

fourth-rank tensor that appears in Equations (8) and (11). Numerically, it can also be obtained by the matrix operations (Cowin and Mehrabadi, 1995) of the six-dimensional representation for a fourth-rank tensor.

### MICROMECHANICAL MODELING

Consider a typical FGM microstructure (Figure 1) containing two phases  $A$  and  $B$  with isotropic elastic stiffness  $\mathbf{C}^A$  and  $\mathbf{C}^B$ , respectively. The global coordinate system of the FGM is denoted by  $(X_1, X_2, X_3)$  with  $X_3$  being the continuous gradation direction. The overall grading thickness of the FGM is  $t$ . Three material zones exist in the gradation direction: Zone I ( $0 \leq X_3 \leq d_1$ ) including phase  $A$  particles with phase  $B$  matrix, the Zone III ( $d_2 \leq X_3 \leq t$ ) including phase  $B$  particles with phase  $A$  matrix, and the transition Zone II ( $d_1 \leq X_3 \leq d_2$ ). When the FGM is subjected to a uniform far-field stress  $\boldsymbol{\sigma}^0$  applied on the  $X_3$  boundary, the averaged stress in each  $X_1$ – $X_2$  layer should be the same as  $\boldsymbol{\sigma}^0$ , based on the equilibrium condition. The averaged stress and strain in the  $X_1$ – $X_2$  layer are defined as the volume average of the stress and strain on the two phases, and are expressed as

$$\boldsymbol{\sigma}^0 = \phi(X_3)\mathbf{C}^A : \langle \boldsymbol{\varepsilon} \rangle^A(X_3) + [1 - \phi(X_3)]\mathbf{C}^B : \langle \boldsymbol{\varepsilon} \rangle^B(X_3), \quad (12)$$

$$\langle \boldsymbol{\varepsilon} \rangle(X_3) = \phi(X_3)\langle \boldsymbol{\varepsilon} \rangle^A(X_3) + [1 - \phi(X_3)]\langle \boldsymbol{\varepsilon} \rangle^B(X_3). \quad (13)$$

For any macroscopic material point  $\mathbf{X}^0$  (Figure 1(a)) in the range of  $0 \leq X_3 \leq d_1$  (Zone I), the corresponding microstructural RVE (Figure 1(b)) contains a number of microparticles of the phase  $A$  embedded in a continuous matrix of the phase  $B$  so that the overall volume fraction of particle phase  $A$  and the its gradient should be consistent with the macroscopic counterparts  $\phi(X_3^0)$  and  $d\phi/dX_3|_{X_3=X_3^0}$ . The microscopic coordinate system  $(x_1, x_2, x_3)$  is constructed with the origin corresponding to  $\mathbf{X}^0$ . All microparticles are assumed to be spherical with identical radius  $a$ . The whole RVE domain is denoted as  $\mathcal{D}$  and the  $i$ th microparticle ( $i = 1, 2, 3, \dots, \infty$ ) domain is denoted as  $\Omega_i$  centered at  $\mathbf{x}^i$ . For the ease of formulation, a particle centered at the origin is assumed and denoted as  $\Omega_0$ .

We use the averaged strain of this particle to represent the averaged particle strain at  $X_3^0$  in the global coordinates. Because a very large number of particles are randomly distributed in the RVE, it is not feasible to directly calculate the local field and then solve the averaged field on the particle. Using the approximation of the pair-wise interaction, we can write the averaged strain in the central particle  $\Omega_0$  in two parts: the elastic-mismatch interaction between the central particle and the matrix (Equation (7)) and

the pair-wise interaction between the central particle and all other particles (Equation (10)):

$$\langle \boldsymbol{\varepsilon} \rangle^A(\mathbf{0}) = (\mathbf{I} - \mathbf{P}_0 \cdot \Delta \mathbf{C})^{-1} : \langle \boldsymbol{\varepsilon} \rangle^B(\mathbf{0}) + \sum_{i=1}^{\infty} \mathbf{d}(\mathbf{0}, \mathbf{x}^i), \quad (14)$$

where  $\langle \boldsymbol{\varepsilon} \rangle^B(\mathbf{0})$  is the averaged matrix strain in the layer with  $x_3=0$ , and the pair-wise interaction reads

$$\mathbf{d}(\mathbf{0}, \mathbf{x}^i) = \Delta \mathbf{C}^{-1} \cdot \mathbf{L}(\mathbf{0}, \mathbf{x}^i) : \langle \boldsymbol{\varepsilon} \rangle^B(x_3^i) + O(\rho^\delta), \quad (15)$$

with  $\langle \boldsymbol{\varepsilon} \rangle^B(x_3^i)$  being the averaged matrix strain tensor in the  $x_3^i$ th- layer. Using ensemble average procedure (Yin et al., 2004), the interactions from all other particles are finally derived as

$$\langle \mathbf{d} \rangle(\mathbf{0}) = \phi(X_3^0) \Delta \mathbf{C}^{-1} \cdot \mathbf{D}(\mathbf{0}) : \langle \boldsymbol{\varepsilon} \rangle^B(\mathbf{0}) + \phi_{,3}(X_3^0) \Delta \mathbf{C}^{-1} \cdot \mathbf{F}(\mathbf{0}) : \langle \boldsymbol{\varepsilon} \rangle_{,3}^B(\mathbf{0}). \quad (16)$$

where,

$$\begin{aligned} \mathbf{D}(\mathbf{0}) &= \int_D \frac{3g(x)}{4\pi a^3} \mathbf{L}(\mathbf{0}, \mathbf{x}) \, d\mathbf{x} \\ \mathbf{F}(\mathbf{0}) &= \int_D e^{-x/\delta} \frac{3g(x)}{4\pi a^3} \mathbf{L}(\mathbf{0}, \mathbf{x}) x_3^2 \, d\mathbf{x} \end{aligned} \quad (17)$$

in which  $\delta$  denotes the attenuating rate of gradation of the particle volume fraction in far field (Yin et al., 2004), and  $g(x)$  the radial distribution function of particles (Percus and Yevick, 1958) with  $x = |\mathbf{x}|$ .

The above two integration terms  $\mathbf{D}$  and  $\mathbf{F}$  can be further simplified and numerically calculated (Yin et al., 2004). Substituting Equation (16) into Equation (14) and recognizing that the origin of the local coordinates in the RVE corresponds to the global coordinate point  $\mathbf{X}^0$  of FGM, we can obtain the averaged particle strain in terms of the arbitrary material point  $X_3$

$$\begin{aligned} \langle \boldsymbol{\varepsilon} \rangle^A(X_3) &= (\mathbf{I} - \mathbf{P}_0 \cdot \Delta \mathbf{C})^{-1} : \langle \boldsymbol{\varepsilon} \rangle^B(X_3) + \phi(X_3) \Delta \mathbf{C}^{-1} \cdot \mathbf{D}(X_3) : \langle \boldsymbol{\varepsilon} \rangle^B(X_3) \\ &\quad + \phi_{,3}(X_3) \Delta \mathbf{C}^{-1} \cdot \mathbf{F}(X_3) : \langle \boldsymbol{\varepsilon} \rangle_{,3}^B(X_3). \end{aligned} \quad (18)$$

In the particle-matrix zone with  $0 \leq X_3 \leq d_1$ , the boundary at  $X_3=0$  corresponds to the 100% matrix material (i.e.,  $\phi(0) = 0$ ). The corresponding boundary conditions can be proposed as

$$\langle \boldsymbol{\varepsilon} \rangle^B(\mathbf{0}) = \mathbf{C}^{B^{-1}} : \boldsymbol{\sigma}^0. \quad (19)$$

With the combination of Equations (12) and (18) and boundary condition (Equation (19)), the averaged strain tensors in both phases can be numerically solved on the basis of the standard backward Eulerian method. Similarly, in the other particle-matrix with the range of  $d_2 \leq X_3 \leq t$  (zone III), we can also calculate the averaged strain fields by the switch of matrix and particle phases.

For the transition zone II ( $d_1 < X_3 < d_2$ ), a phenomenological transition function (Yin et al., 2004) is introduced as

$$f(X_3) = \left[ 1 - 2 \frac{\phi(X_3) - \phi(d_1)}{\phi(d_1) - \phi(d_2)} \right] \left[ \frac{\phi(X_3) - \phi(d_2)}{\phi(d_1) - \phi(d_2)} \right]^2, \quad (20)$$

so that the averaged strain of each phase ( $A$  or  $B$ ) in the transition zone II can be approximated as a cubic Hermite function. Thus, the averaged strain of the same phase ( $A$  or  $B$ ) from two particle-matrix zones (zones I and III) is given by

$$\langle \mathbf{e} \rangle_{\text{zone-II}}^{A \text{ or } B}(X_3) = f(X_3) \langle \mathbf{e} \rangle_{\text{zone-I}}^{A \text{ or } B}(X_3) + [1 - f(X_3)] \langle \mathbf{e} \rangle_{\text{zone-III}}^{A \text{ or } B}(X_3). \quad (21)$$

The overall averaged strain tensor at each layer in the transition zone can be further obtained from Equation (13). However, because the microstructure of the transition zone is not truly characterized, this treatment only provides a phenomenological approximation for the averaged strain in the transition instead of a rigorous solution. To accurately predict the effective material properties in the transition zone, a rigorous characterization of the microstructure is ultimately needed (Torquato, 2002).

## DAMAGE MODELING

When the applied loading  $\sigma^0$  is small, the particles are perfectly bonded to the matrix. However, with increase of applied load, the interfacial normal stress can reach the interfacial debonding strength so that the particles start to debond from the matrix. The stress on the debonded surface area is released with extra deformation allowed. Thus, the effective stiffness of the particles reduces as a result of the increase of debonding area. In the present damage model, when partial interfacial debonding occurs, the equivalent stiffness method (Zhao and Weng, 2002; Liu et al., 2004) is introduced; i.e., the partially debonded isotropic particles are replaced by fictitious orthotropic yet perfectly bonded particles. Consequently, the above micromechanical analysis is still applicable.

For simplicity, the averaged stress of particles is assumed to represent the interfacial stress so that the interfacial normal stress is expressed as

$$\sigma^{\text{normal}} = \mathbf{t}^T \cdot \bar{\boldsymbol{\sigma}} \cdot \mathbf{t} \tag{22}$$

where  $\mathbf{t}$  is the unit outward normal vector at any point along the interface. By comparing the interfacial normal stress with the interfacial debonding strength  $\sigma_{\text{cri}}$  at any surface point, we can solve the debonding area on the surface of the particle as a function of debonding angles to the directions of the three principal stresses ( $\sigma_1, \sigma_2, \sigma_3$ ) in the particles. Initially, the loading is small so that all the principal stresses are less than the interfacial strength. Thus, all the particles are fully bonded and no debonding process is activated. With further increase in the far-field loading, the interfacial debonding may occur in the interfacial area with the interfacial normal stress larger than the interfacial strength. Following the previous work (Liu et al., 2004) for composite materials, the interfacial debonding spreads in the following three categories. In each category, for one-eighth of a particle with structural symmetry, the debonding area is described by two debonding angles, which are defined in terms of the principal stresses and the interfacial strength and vary in the range of  $0-\pi/2$  (Liu et al., 2004). Three damage parameters  $D_i$  ( $i=1,2,3$ ), projections of the debonding area in three principal directions normalized by the total projected area, are derived to evaluate the loss of the particles' tensile load-transfer capacity for each category.

**Category 1**  $\sigma_1 \geq \sigma_{\text{cri}} \geq \sigma_2 \geq \sigma_3$

Only the first principal stress is greater than the interfacial strength  $\sigma_{\text{cri}}$ . The interfacial debonding initiates from the first principal direction, which corresponds to the white area on the surface of the particle in Figure 2(b), and propagates toward the other two principal directions. Figure 2(c) shows one-eighth of the debonded particle. Here,  $A_2, B_2,$  and  $C_2$  denote the projections of the debonded area onto the three midplanes of  $x_2-x_3, x_3-x_1,$  and  $x_1-x_2,$  respectively; and  $A_1, B_1,$  and  $C_1$  denote the corresponding projections of the unbonded area. Therefore,  $A_1 + A_2 = B_1 + B_2 = C_1 + C_2 = \pi a^2/4$ . The three damage parameters are expressed as

$$D_1 = \frac{A_2}{\pi a^2/4} = \frac{\sigma_1 - \sigma_{\text{cri}}}{\sqrt{(\sigma_1 - \sigma_2)(\sigma_1 - \sigma_3)}}$$

$$D_2 = \frac{B_2}{\pi a^2/4} = \frac{2}{\pi} \left( \arcsin \sqrt{\frac{\sigma_1 - \sigma_{\text{cri}}}{\sigma_1 - \sigma_3}} - \sqrt{\frac{\sigma_1 - \sigma_{\text{cri}}}{\sigma_1 - \sigma_3}} \sqrt{\frac{\sigma_{\text{cri}} - \sigma_2}{\sigma_1 - \sigma_2}} \right)$$

$$D_3 = \frac{C_2}{\pi a^2/4} = \frac{2}{\pi} \left( \arcsin \sqrt{\frac{\sigma_1 - \sigma_{\text{cri}}}{\sigma_1 - \sigma_2}} - \sqrt{\frac{\sigma_1 - \sigma_{\text{cri}}}{\sigma_1 - \sigma_2}} \sqrt{\frac{\sigma_{\text{cri}} - \sigma_3}{\sigma_1 - \sigma_3}} \right). \tag{23}$$

**Category 2**  $\sigma_1 \geq \sigma_2 \geq \sigma_{\text{cri}} \geq \sigma_3$

Two principal stresses are greater than the interfacial strength  $\sigma_{\text{cri}}$ . The interfacial debonding propagates around the particle, which corresponds to the gray area on the surface of the particle in Figure 2(b), but still bond to the matrix along two ends in the other principal direction. In Figure 2(c),  $A_1$ ,  $B_1$ , and  $C_1$  denote the projections of the debonded area onto the three midplanes of  $x_2 - x_3$ ,  $x_3 - x_1$ , and  $x_1 - x_2$ , respectively. As a result, the three damage parameters are obtained as

$$\begin{aligned} D_1 &= \frac{B_1}{\pi a^2/4} = \frac{2}{\pi} \left( \arcsin \sqrt{\frac{\sigma_2 - \sigma_{\text{cri}}}{\sigma_2 - \sigma_3}} + \sqrt{\frac{(\sigma_1 - \sigma_{\text{cri}})(\sigma_{\text{cri}} - \sigma_3)}{(\sigma_1 - \sigma_3)(\sigma_2 - \sigma_3)}} \right) \\ D_2 &= \frac{C_1}{\pi a^2/4} = \frac{2}{\pi} \left( \arcsin \sqrt{\frac{\sigma_1 - \sigma_{\text{cri}}}{\sigma_1 - \sigma_3}} + \sqrt{\frac{(\sigma_2 - \sigma_{\text{cri}})(\sigma_{\text{cri}} - \sigma_3)}{(\sigma_1 - \sigma_3)(\sigma_2 - \sigma_3)}} \right). \tag{24} \\ D_3 &= \frac{A_1}{\pi a^2/4} = 1 - \frac{\sigma_{\text{cri}} - \sigma_3}{\sqrt{(\sigma_1 - \sigma_3)(\sigma_2 - \sigma_3)}} \end{aligned}$$

**Category 3**  $\sigma_1 \geq \sigma_2 \geq \sigma_3 \geq \sigma_{\text{cri}}$

In this case, all principal stresses exceed the interfacial strength. Thus, the entire interface is debonded as a void and the particle cannot transfer any tensile loading. The damage parameters are written as

$$D_1 = D_2 = D_3 = 1. \tag{25}$$

With the increase in the damage of particles, a larger deformation is permitted and thus the overall composite becomes more compliant. To simulate the stiffness reduction, the damaged particle is replaced by the fully bonded one, but with reduced stiffness in certain directions corresponding to the damage parameters. Thus, the equivalent stiffness tensor of the damaged particle is orthotropic

$$\tilde{C}_{ijkl}^{AorB} = \lambda_{IK}^{AorB} \delta_{ij} \delta_{kl} + \mu_{IJ}^{AorB} (\delta_{ik} \delta_{jl} + \delta_{il} \delta_{jk}), \tag{26}$$

where,

$$\lambda_{IK}^{AorB} = \lambda^{AorB}(1 - D_I)(1 - D_K), \quad \mu_{IJ}^{AorB} = \mu^{AorB}(1 - D_I)(1 - D_J), \quad (27)$$

with the particle as either phase *A* or phase *B*. It is noted that Mura's (1987) tensorial indicial notation is followed in Equation (26); i.e., uppercase indices have the same representation as the corresponding lowercase ones but are not summed.

Because the reference coordinates for the stiffness tensor in Equation (26) are in the principal directions of the local stress, it should be transferred back to the global coordinates. Cowin and Mehrabadi's (1995) formulas of six-dimensional representation for a three-dimensional tensor are employed. The rotation and inverse of a fourth-rank tensor can be done with the matrix form in the six-dimensional space.

## NUMERICAL SIMULATIONS AND DISCUSSION

To numerically calculate the effect of progressive interfacial debonding on the effective elastic behavior of FGMs, a loading-control algorithm is proposed. Given a uniform loading on the upper and lower boundaries of the FGM, we first obtain the boundary condition in Equation (19). In the particle-matrix zone, we calculate the averaged strain in particles by Equation (18) for the given layer with  $X_3 > 0$ , and then obtain the principal stresses in the particles. The interfacial debonding occurs when the maximum principal stress exceeds the interfacial debonding strength. Using Equations (23)–(27), we further solve the damage parameters, and then update equivalent elasticity of the particles at that layer. Using the updated elasticity of the particles, we recalculate the particle averaged stress and check the interfacial debonding again until the maximum principal stress is equal to the interfacial strength. Finally we solve the averaged strain and stress at that layer, with which, we obtain the averaged elastic fields in the particle-matrix zones I and III. In the transition zone II, we employ Equations (20) and (21) to solve the averaged strains. Therefore, we eventually obtain the elastic field distributions in the FGM, which are continuous and differentiable.

To test the effective elasticity at any loading condition, an extra infinitesimal testing stress is applied on the lower and upper FGM boundaries, and then the averaged strain distribution in the gradation direction is calculated from the above algorithm. From the relation between the testing stress and the increment of the averaged strain, we calculate the effective elasticity distribution. For instance, given a small uniaxial testing

loading  $\Delta\sigma_{33}$  on the lower and upper FGM boundaries, we solve the increment of the averaged strain as  $\Delta\varepsilon(X_3)$ . Then, the effective Young's modulus and the Poisson's ratio at any material layer in the FGM gradation direction can be derived as:

$$E(X_3) = \frac{\Delta\sigma_{33}}{\Delta\varepsilon_{33}(X_3)}; \quad \nu(X_3) = -\frac{\Delta\varepsilon_{11}(X_3)}{\Delta\varepsilon_{33}(X_3)}. \quad (28)$$

The effective shear modulus at any material layer can be similarly obtained through a shear testing loading  $\Delta\tau_{13}$  as:

$$\mu(X_3) = \frac{\Delta\tau_{13}}{2\Delta\varepsilon_{13}(X_3)}. \quad (29)$$

It is noted that we can also apply a testing shear loading  $\Delta\tau_{23}$  to obtain the effective shear modulus in the other direction in the same way. Because all damaged particles in the RVE are approximated by the same orthotropic materials with the same principal directions, the effective elasticity at the material point is expected to be also orthotropic. However, for different RVEs in the gradation direction, the debonding angles of particles may be different, so the change of effective elasticity due to the particle damage spatially varies in the gradation direction. In Equations (28) and (29), three commonly used elastic moduli are calculated. To calculate other effective elastic moduli, we can design the corresponding loadings similarly.

For convenience, the proposed algorithm for computing averaged stress and strain distributions in a particle-matrix zone changing with the progressive interfacial debonding is summarized in Table 1. It is noted that given an FGM and a loading condition, the final averaged strain distribution depends on the loading path due to the irreversible damage of the particles. In this algorithm, we can record the loading and damage history to simulate some complex loading paths.

To demonstrate the capability of the proposed model, two loading types are illustrated: uniaxial loading and shear loading, which correspond to FGMs subjected to negative pressure and frictional loading, respectively. The sample FGM is the C/SiC FGM with the silicon carbide as phase *A* ( $E_A = 320$  GPa,  $\nu_A = 0.3$ ) and the carbon as phase *B* ( $E_B = 28$  GPa,  $\nu_B = 0.3$ ) (Reiter et al., 1997). The interfacial debonding strength is assumed as  $\sigma_{\text{cri}} = 100$  MPa. For the convenience of numerical simulations, the lower and upper bounds  $d_1$  and  $d_2$  are selected where the corresponding volume

**Table 1. Algorithm for computing averaged stress and strain distributions in the particle-matrix zone I with interfacial debonding.**

**Initialize:**

Material constants:  $\sigma_{\text{cri}}$ ;  $\mathbf{C}^A(\lambda_A, \mu_A)$ ;  $\mathbf{C}^B(\lambda_B, \mu_B)$  (phase A: particle; B: matrix)  
 Geometry:  $\phi(X_3)$ ;  $\phi_{,3}(X_3)$ ;  $\mathbf{a}$ ;  $d_1$ ;  $N$  ( $N$ : divisions in the gradation direction)  
 Loading path:  $\sigma^{(1)}$ ,  $\sigma^{(2)}$ , ...,  $\sigma^{(M)}$  ( $M$ : total loading steps)

**Solve:**

**Loading loop:** (solve the averaged strain distribution at each loading step)

$$\sigma^0 = \sigma^{(i)}; \langle \epsilon \rangle^{B(i)}(0) = \mathbf{C}^{B^{-1}} : \sigma^0$$

**Spatial loop:** (solve the averaged strain at each layer in the gradation direction)

Compute  $\langle \epsilon \rangle^{B(i)}(X_3^{(j)})$ ,  $\langle \epsilon \rangle^{A(i)}(X_3^{(j)})$  from Equations (12) and (18)

**Damage check loop:** (check the interfacial debonding and update  $\mathbf{C}^A(X_3^{(j)})$ )

    Compute the principal stresses and directions

    Check debonding type, calculate debonding angles, and update the equivalent stiffness of the particles using Equations (23)–(27)

    Update  $\langle \epsilon \rangle^{B(i)}(X_3^{(j)})$ ,  $\langle \epsilon \rangle^{A(i)}(X_3^{(j)})$  from Equations (12) and (18)

**End damage check loop** (the interfacial normal stress is not larger than  $\sigma_{\text{cri}}$ )

**End spatial loop** (averaged strain distribution at the loading step is solved)

**End loading loop** (final averaged stress and strain distribution is obtained)

fractions are 40 and 60%, respectively, following Bao and Cai’s suggestion (1997). The volume fraction distribution is assumed to be linear.

Under uniaxial tensile loading in the gradation direction, the first principal stress is found to be much larger than the other two equalized principal stresses. The interfacial debonding falls in Category 1. Figure 3(a) shows the particle stress distribution in the gradation direction with applied loading  $\sigma_{33}^0 = 50$  MPa. It is apparent that the first (maximum) principal stress 88 MPa of particles is less than the interfacial strength; thus no interfacial debonding occurs under this loading. Although the external loading is only applied in one direction, a compressive stress can be observed in the particle in the two other directions. In the particle–matrix zone I, as the particles are much stiffer than the matrix, the particle tensile stress is larger than the applied tensile loading. With the increase in the volume fraction of particles, particle averaged stress is reduced. In zone III, the particle and matrix phases are interchanged and, correspondingly, the tendency is totally reversed. In the transition zone II, the solution is obtained from the combination of two cases of particle and matrix zone. As a result, the stresses continuously extend to the corresponding particle-matrix zone for each case, as illustrated by Figure 3(a).

Figure 3(b) and (c) demonstrates the elastic modulus distributions in the gradation direction changing with the tensile loading. For  $\sigma_{33}^0 = 50$  MPa, no interfacial debonding occurs and the effective Young’s modulus and the effective shear modulus increase with the value of  $X_3$  due to the increase

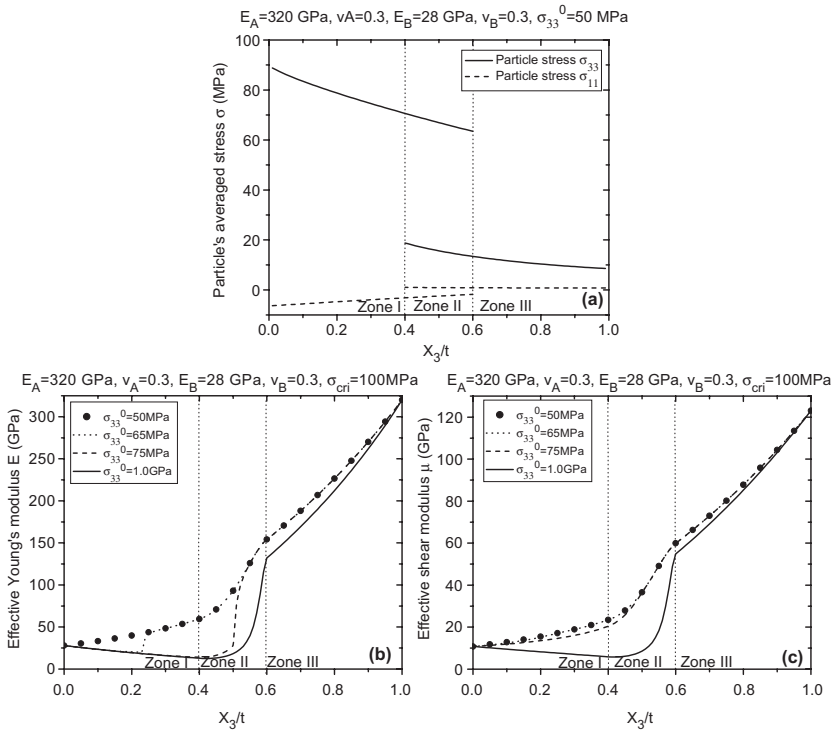


**Figure 3.** Results for the uniaxial tensile loading: (a) particle's averaged stress distribution in the gradation direction in the linear elastic range; (b) effective Young's modulus distribution; and (c) effective shear modulus distribution.

in the volume fraction of phase *A*. For  $\sigma_{33}^0 = 65$  MPa, particles debond in the range of  $0 \leq X_3 \leq 0.24t$  in the zone I, and in this range the effective Young's modulus decreases along with the value of  $X_3$  and rapidly increases to the value  $\sigma_{33}^0 = 50$  MPa at  $X_3 = 0.24t$  due to no debonding; whereas the effective shear modulus still increase and is almost the same as that for  $\sigma_{33}^0 = 50$  MPa. The above observation is due to the fact that the debonding angles are small and the debonding area is along two caps of particles in the loading direction, having a larger projection in the loading direction but much smaller projections in the other two directions. Thus, the effective Young's modulus is reduced much faster than the shear modulus compared with those for the fully bonded condition. For  $\sigma_{33}^0 = 75$  MPa, the debonding range in the FGM becomes larger as  $0 \leq X_3 \leq 0.51t$  and the debonding angles also increase compared with those for  $\sigma_{33}^0 = 65$  MPa. It is seen that the effective shear moduli are still close to those for the fully bonded

condition, whereas the effective Young's moduli have been much reduced. When the loading is as large as 1.0 GPa, all particles in the FGM start to debond and the debonding angles are large especially for zone I. It is therefore shown that both the effective Young's modulus and the effective shear modulus decrease along with the value of  $X_3$  in zone I and then increase in zone III.

It should be noted that, while tensile load-transfer capacity in particles decreases with the interfacial debonding, the matrix can sustain the trade-off loading. In this work, because we do not consider the strength of each phase, even though the particles are totally debonded, the mechanical behavior of this material is equivalent to the corresponding matrix containing voids. Although we are indicating the C/SiC material system, the properties are being used just for the sake of reference. The damage pattern and mechanisms observed with our model are not necessarily the ones associated with the real material system. In reality, the carbon phase does not sustain loading as high as 1.0 GPa. To show the particle interfacial debonding in the silicon-carbide-rich end, we assume the bulk materials of each phase to be strong enough and ignore possible damage other than the interfacial debonding. Thus, the material will not lose its stability and the effective elasticity is always positive though it keeps decreasing with extra loading. Apparently, in zone III of Figure 3, because the phase-*B* particles are much more compliant than the phase-*A* matrix, even though the particles are reduced to voids, the effective elasticity does not change much.

To illustrate the evolution of particle's debonding angles, Figure 4(a) shows the debonding angles in zone I for four loading cases. With the increase of the tensile loading, particles start to debond at the bottom of the FGM because the average particle tensile stress is maximum at the bottom. For  $\sigma_{33}^0 = 50$  MPa, no debonding is observed; whereas for the other three cases, we can see particle's debonding angles varying in the gradation direction. In the specific cases of  $\sigma_{33}^0 = 65$  MPa and 75 MPa, the debonding angles of the particles in the zone I decrease along with the value of  $X_3$  because the particle averaged stress is reduced. However, when the tensile loading increases, the damage of the particles becomes more severe, and the equivalent stiffness of the particles may even be more compliant than the matrix, so the debonding angles increase along with the value of  $X_3$  for  $\sigma_{33}^0 = 1.0$  GPa. Figure 4(b) and (c) shows the debonding angles at  $X_3/t = 0.2$  for different loading cases and for  $\sigma_{33}^0 = 65$  MPa at different locations, which are marked in Figure 4(a). We observe that the debonding angle variation with the loading and location is more sensitive when the debonding angle is small. If the debonding angle of a particle is large, a small extra loading will not considerably change the debonding angle.

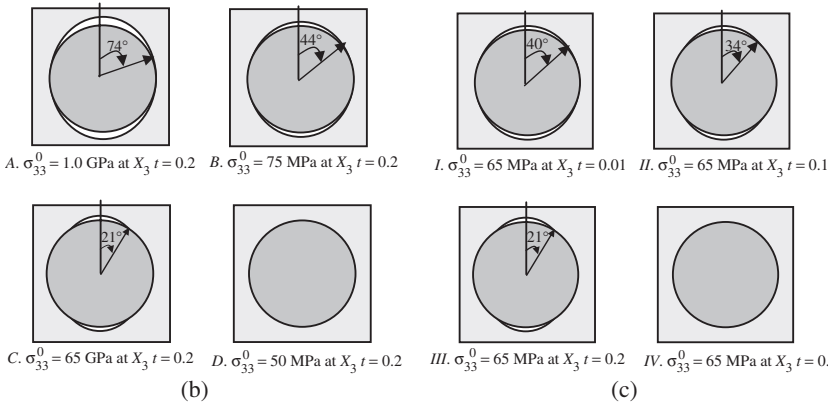
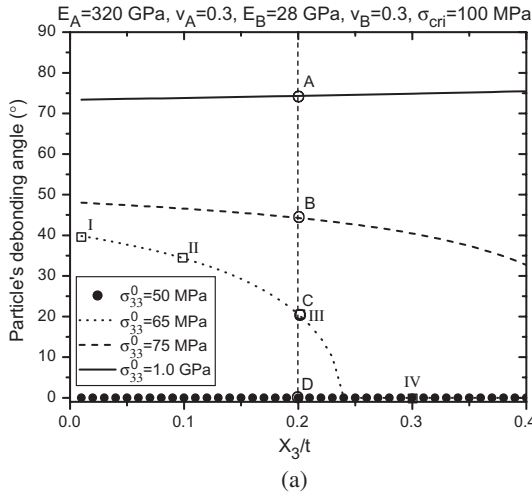


**Figure 4.** Evolution of particle's debonding angles under uniaxial tensile loading: (a) particle debonding angles in Zone I for different loading cases; (b) illustration of debonding angles at  $X_3/t = 0.2$ ; and (c) illustration of debonding angles for  $\sigma_{33}^0 = 65\text{MPa}$ .

Shear loading is further considered. Under shear loading on the upper and lower boundaries ( $\tau_{13}^0 > 0$ ), we observe that the three principal stresses in the particles are tensile, zero, and compressive, respectively. The interfacial debonding should also initiate from Category 1. However, the local principal coordinates are no longer consistent with the global coordinates and need to rotate  $\pi/4$  around the  $X_2$ -axis. The debonding area is along two caps in the first principal direction instead of  $X_3$ -axis. Moreover, because the second and the third principal stresses are not equal, the shear modulus in the  $X_1-X_3$  plane and that in the  $X_2-X_3$  plane are no longer the same.

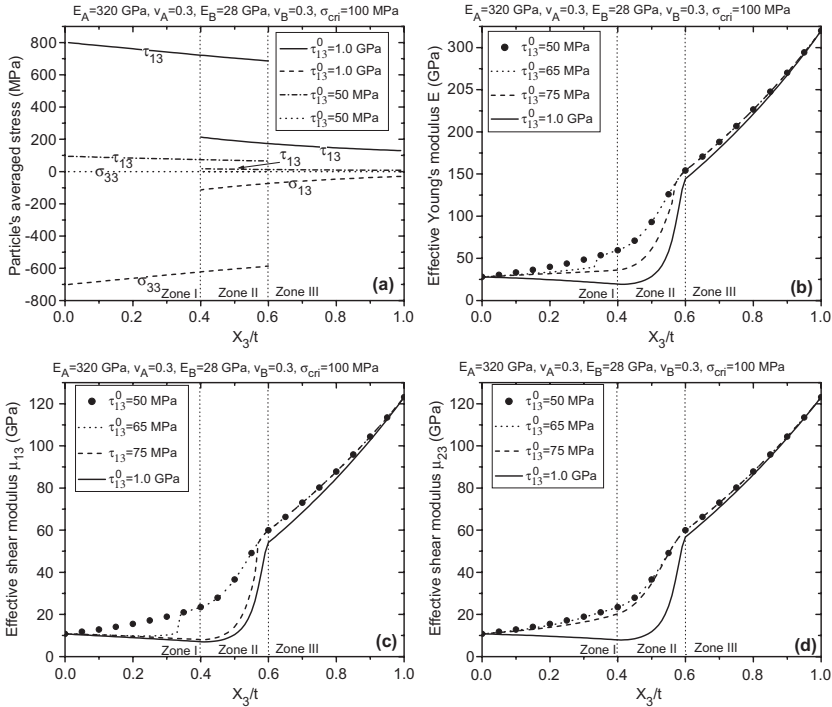


**Figure 5.** Results for the shear loading: (a) particle's averaged stress distribution in the gradation direction; (b) effective Young's modulus distribution; (c) effective shear modulus distribution in the  $X_1$ – $X_3$  plane; and (d) effective shear modulus distribution in the  $X_2$ – $X_3$  plane.

Figure 5(a) shows the particle stress distribution in the gradation direction with two values of applied shear loading. For  $\tau_{13}^0 = 50$  MPa, in an average sense only the stress component  $\tau_{13}$  is nonzero in particles of the FGM, and thus the first (maximum) particle's averaged stress is equal to the shear stress. It is seen to be less than the interfacial strength so that no debonding occurs. However, for  $\tau_{13}^0 = 1.0$  GPa, all particles start to debond, and the equivalent stiffness of particles are strongly anisotropic due to the severe debonding. A nonzero stress  $\sigma_{33}$  is observed.

Figure 5(b)–(d) demonstrates the evolution processes of the effective Young's modulus  $E$ , the shear modulus  $\mu_{13}$  in the  $X_1$ – $X_3$  plane, and the shear modulus  $\mu_{23}$  in the  $X_2$ – $X_3$  plane, respectively, under various shear loading  $\tau_{13}^0$  values. When  $\tau_{13}^0$  increases from 50 to 65 MPa, particles start to debond in the range of  $0 \leq X_3 \leq 0.34 t$ . Thus both  $E$  and  $\mu_{13}$  are considerably reduced; whereas  $\mu_{23}$  remains approximately the same. For  $\tau_{13}^0 = 65$  MPa,  $\mu_{13}$  decreases along with the value of  $X_3$  in the range of  $0 \leq X_3 \leq 0.34 t$  due to

the debonding, but  $E$  and  $\mu_{23}$  still keep increasing. When  $\tau_{13}^0$  continuously increases from 65 to 75 MPa and 1.0 GPa, though the effective shear modulus  $\mu_{13}$  in the debonded range keeps decreasing, the change is small; whereas  $E$  and  $\mu_{23}$  change more obviously with the loading. Comparing Figures 3(b) and 5(b), one can observe that the effective Young's modulus decreases faster along with the uniaxial tensile loading than with the shear loading, but vice versa for the effective shear modulus  $\mu_{13}$ . It is noted that the shear modulus in all directions is the same under the uniaxial tensile loading, and thus  $\mu_{13} = \mu_{23} = \mu$ .

## CONCLUSIONS

A micromechanics-based damage framework is proposed for two-phase FGMs to characterize how the process of interfacial debonding between particles and the matrix affects the overall elastic behavior of the FGMs. The averaged elastic field distributions in the gradation direction are derived by considering the pair-wise interactions between particles for the FGM under uniform mechanical loading on its upper and lower boundaries. When particle's normal interfacial stress is greater than the interfacial debonding, the damage evolution is described by the debonding angle-related damage parameters varying with the external loading. The elastic equivalence is constructed by replacing debonded particles with the perfectly bonded yet orthotropic particles. Numerical simulations demonstrate that the effective elastic moduli becomes more compliant due to debonding damage. Under uniaxial tensile loading, the effective Young's modulus decreases faster than the effective shear modulus. Under shear loading, the effective shear modulus within the same plane as the loading decreases faster than the effective Young's modulus and the effective shear modulus in another plane.

In this model, both phases of FGMs are assumed to be elastic materials. The strength of each phase is high enough that the damage within the particles or the matrix is not considered. Although this may be a reasonable approximation for some FGMs under intermediate loading condition, consideration of inelasticity (e.g., metal phase exhibiting plasticity) and fracture (e.g., ceramic phase) is ultimately needed. Because FGMs have been widely used as thermal protection systems under multicycles of thermal loading, future modeling efforts are planned to investigate interfacial debonding due to the thermo-mechanical loading and simulate hysteresis behavior of FGMs due to fatigue loading. The current results may also be used in fracture and damage simulations of FGMs, in which the FGMs are treated as homogenized materials with a spatially varying elasticity provided by the proposed model.

In summary, although some reasonable results are obtained, the proposed model is still subjected to the following limitations:

1. Two-phase FGMs with one-dimensional material gradient is considered, and both phases are assumed to be isotropic elastic materials;
2. Particles in the RVE are assumed to be spherical with the same size;
3. The damage of particles in the same RVE is assumed to be identical, which may not reflect the stochastic process of damage for a many-particle system;
4. For the debonded interface, the compressive loading is not considered, so the combined loading path with both compression and tension cannot be simulated by this model;
5. In the transition zone, the mechanical solution is approximated by a phenomenological method instead of a physics-based mechanical derivation.

### ACKNOWLEDGMENT

This work is sponsored by the National Science Foundation under grant numbers CMS-0084629 and CMS-0333576. The support is gratefully acknowledged.

### REFERENCES

- Aboudi, J., Pindera, M.-J. and Arnold, S.M. (1999). Higher-order Theory for Functionally Graded Materials, *Compos. B*, **30**(8): 777–832.
- Bao, G. and Cai, H. (1997). Delamination Cracking in Functionally Graded Coating/Metal Substrate Systems, *Acta Mater.*, **45**(3): 1055–1066.
- Cowin, S.C. and Mehrabadi, M.M. (1995). Anisotropic Symmetries of Linear Elasticity, *Appl. Mech. Rev.*, **48**(5): 247–285.
- Dvorak, G.J. and Zhang, J. (2001). Transformation Field Analysis of Damage Evolution in Composite Materials, *J. Mech. Phys. Solids*, **49**(11): 2517–2541.
- Eshelby, J.D. (1957). The Determination of the Elastic Field of an Ellipsoidal Inclusion, and Related Problems, *Proc. Roy. Soc.*, **A241**(1226): 376–396.
- Jasiuk, I. and Tong, Y. (1989). The Effect of Interface on the Elastic Stiffness of Composites, In: Reddy, J.N. and Tepy, J.L. (eds), *Proc. 3rd Joint ASCE/ASME Mech. Conf.*, pp. 49–54.
- Ju, J.W. and Chen, T.M. (1994). Effective Elastic Moduli of Two-phase Composites Containing Randomly Dispersed Spherical Inhomogeneities, *Acta Mech.*, **103**(1–4): 123–144.
- Kröner, E. (1990). Modified Green Functions in the Theory of Heterogeneous and/or Anisotropic Linearly Elastic Media, In: Weng, G.J., Taya, M., Abé, H., (eds), *Micromechanics and Inhomogeneity*, pp. 197–211, Springer-Verlag, New York.
- Liu, H.T., Sun, L.Z. and Ju, J.W. (2004). An Interfacial Debonding Model for Particle-reinforced Composites, *Inter. J. Damage Mech.*, **13**(2): 163–185.
- Matous, K. (2003). Damage Evolution In Particulate Composite Materials, *Inter. J. Solids Struct.*, **40**(6): 1489–1503.

- Miyamoto, Y., Kaysser, W.A., Rabin, B.H., Kawasaki, A. and Ford, R.G. (1999). *Functionally Graded Materials: Design, Processing and Applications*, Kluwer Academic Publishers, Dordrecht.
- Moschovitsis, Z.A. and Mura, T. (1975). Two-ellipsoidal Inhomogeneities by the Equivalent Inclusion Method, *ASME Journal of Applied Mechanics*, **42**(4): 847–852.
- Mura, T. (1987). *Micromechanics of Defects in Solids*, **2nd edn**, Kluwer Academic Publishers, Dordrecht.
- Nemat-Nasser, S. and Hori, M. (1999). *Micromechanics: Overall Properties of Heterogeneous Materials*, **2nd edn**, North-Holland, London.
- Paulino, G.H., Jin, Z.H. and Dodds, R.H. (2003). Failure of Functionally Graded Materials, In: Karihaloo, B. and Knauss, W.G. (eds), *Comprehensive Structural Integrity*, Vol. 2, pp. 607–644, Elsevier Science Publisher, Amsterdam.
- Percus, J.K. and Yevick, G.J. (1958). Analysis of Classical Statistical Mechanics by Means of Collective Coordinates, *Phys. Rev.*, **110**(1): 1–13.
- Prader, P. and Degisher, H.P. (1999). Thermal Cycling Creep of Particle Reinforced Aluminum, In: *Proc. 12th Internat. Conf. Compos. Mater.*, ICCM12, Paris, p. 644.
- Qu, J. (1993). The Effect of Slightly Weakened Interfaces on the Overall Elastic Properties of Composite Materials, *Mechanics of Materials*, **14**(4): 269–281.
- Reiter, T. and Dvorak, G.J. (1998). Micromechanical Models for Graded Composite Materials: II. Thermomechanical Loading, *Journal of the Mechanics Physics of Solids*, **46**(9): 1655–1673.
- Reiter, T., Dvorak, G.J. and Tvergaard, V. (1997). Micromechanical Models for Graded Composite Materials, *Journal of the Mechanics Physics of Solids*, **45**(8): 1281–1302.
- Sangani, A.S. and Mo, G. (1997). Elastic Interactions in Particulate Composites with Perfect as Well as Imperfect Interfaces, *J. Mech. Phys. Solids*, **45**(11–12): 2001–2031.
- Sasaki, M. and Hirai, T. (1991). Fabrication and Properties of Functionally Gradient Materials, *J. Ceram. Soc. Jap.*, **99**(10): 1002–1013.
- Sun, L.Z., Ju, J.W. and Liu, H.T. (2003). Elastoplastic Modeling of Metal Matrix Composites with Evolutionary Particle Debonding, *Mech. Mater.*, **35**(3–6): 559–569.
- Suresh, S. and Mortensen, A. (1998). *Fundamentals of Functionally Graded Materials*, IOM Communications Ltd, London.
- Suresh, S., Mortensen, A. and Needleman, A. (1993). *Fundamentals of Metal-Matrix Composites*, Butterworth-Heinemann Publisher, Boston.
- Torquato, S. (2002). *Random Heterogeneous Materials: Microstructure and Macroscopic Properties*, Springer-Verlag, New York.
- Voyiadjis, G.Z. and Park, T. (1997). Local and Interfacial Damage Analysis of Metal Matrix Composites Using the Finite Element Method, *Eng. Fract. Mech.*, **56**(4): 483–511.
- Yin, H.M., Sun, L.Z. and Paulino, G.H. (2004). Micromechanics-based Elastic Model for Functionally Graded Materials with Particle Interactions, *Acta Mater*, **52**(12): 3535–3543.
- Yin, H.M., Sun, L.Z. and Paulino, G.H. (2005). A Multiscale Framework for Elastic Deformation of Functionally Graded Composites, *Mater. Sci. Forum*, **492–493**: 391–396.
- Zhao, Y.H. and Weng, G.J. (1996). Plasticity of a Two-Phase Composite with Partially Debonded Inclusions, *Int. J. Plastic*, **12**(6): 781–804.
- Zhao, Y.H. and Weng, G.J. (1997). Transversely Isotropic Moduli of Two Partially Debonded Composites, *Int. J. Solids Struct.*, **34**(4): 493–507.
- Zhao, Y.H. and Weng, G.J. (2002). The Effect of Debonding Angle on the Reduction of Effective Moduli of Particle and Fiber-reinforced Composites, *J. Appl. Mech.*, **69**(3): 292–302.
- Zuiker, J.R. (1995). Functionally Graded Materials – Choice of Micromechanics Model and Limitations in Property Variation, *Compos. Eng.*, **5**(7): 807–819.
- Zuiker, J.R. and Dvorak, G.J. (1994). The Effective Properties of Functionally Graded Composites – I. Extension of the Mori-Tanaka Method to Linearly Varying Fields, *Compos. Eng.*, **4**(1): 19–35.